Segmentation of SAR Intensity Imagery With a Voronoi Tessellation, Bayesian Inference, and Reversible Jump MCMC Algorithm

Yu Li, Jonathan Li, *Member, IEEE*, and Michael A. Chapman

***Abstract*—This paper presents a region-based approach to segmentation of the satellite synthetic aperture radar (SAR) intensity imagery. The approach is based on a Voronoi tessellation, the Bayesian inference, and the reversible jump Markov chain Monte Carlo (RJMCMC) algorithm. By Voronoi tessellation, the approach partitions a SAR image into a set of polygons corresponding to the components of the segmented homogenous regions. Each polygon is assigned a label to indicate a homogeneous region. The labels for all the polygons form a label field, which is characterized by an improved Potts model. The intensities of pixels in each polygon are assumed to satisfy identical and independent gamma distributions in terms of their label. Following the Bayesian paradigm, the posterior distribution that characterizes the SAR image segmentation can be obtained up to the integration constant. Then, a RJMCMC scheme is designed to simulate the posterior distribution and estimate its parameters. Finally, an optimal segmentation is obtained by the maximum *a posteriori* algorithm. The results obtained on both real Radarsat-1/2 and simulated SAR intensity images show that our approach works well and is very promising.**

***Index Terms*—Bayesian inference, image segmentation, maximum *a posteriori* (MAP), reversible jump Markov chain Monte Carlo (RJMCMC), synthetic aperture radar (SAR), Voronoi tessellation.**

I. Introduction

GENERALLY speaking, segmentation of remotely sensed data is a procedure of partitioning a given scene into meaningful regions that correspond to land use and land cover (LULC) classes or a part of them in the scene. To this end, it is necessary to investigate the imaging properties of LULC classes and infer constraints to characterize them. The challenges lie in translating these constraints into criteria applicable at data level, e.g., modeling the segmentation problem by using these criteria and proposing a scheme to obtain an optimal segmentation for a given data set. Perhaps the most commonly used criterion is homogeneity, which is derived from Marr's idea on the coherency of matter [1]. In the data processing of satellite synthetic aperture radar (SAR) intensity imagery (hereafter referred to as the SAR imagery), segmentation is the most critical task as the quality of the segmentation stage is essential for further high-level data processing tasks such as feature extraction, object recognition, and classification. It also has prominent effects on the global quality of all remotely sensed data interpretation system [2]. SAR image segmentation is by far still a very difficult task. The difficulties stem from both the intractability of the segmentation problem itself and the effect of speckle noise in SAR imagery. According to [3], a mathematical problem is well posed only if its solution exists and is unique and robust to noise. While SAR imaging is shown to be a well-posed direct problem, SAR image segmentation is considered as an inverse ill-posed problem since its solution is usually not unique [4]. The speckle phenomenon due to the *coherent* nature of *radar backscatters* in SAR imagery [5] causes inaccurate measurements of backscatter coefficients, which is proportional to the measured power of the received microwave given by the square of its amplitude. Several techniques have been developed for suppressing speckle noise [2]. The more commonly used technique is known as multilooking [2], [5]. In this technique, the Doppler spectrum is equivalently split into several adjacent subsets, each of which occupies a different part of the Doppler spectrum. Each of these subsets can be used to form a separate image (or a look). Then, by averaging the looks on power, the radiometric accuracy of the measurements is improved but at the cost of resolution [2].

Following the above multilook processing, there are numerous algorithms for SAR image segmentation published in the literature. All of them can broadly be *categorized into three groups*: 1) clustering-based segmentation algorithm [6]–[9]; 2) edge-based segmentation algorithm [10], [11]; and 3) region-based segmentation algorithm [12]–[15].

The Markov random field (MRF) provides a mathematical formulation for modeling local spatial interactions between locations. Currently, MRF has been proved to be a powerful tool for solving the SAR image segmentation problem by taking into account the multiplicative nature of speckle noise in a statistically optimal way and also provides an efficient regularization framework [16]. Various MRF models have been developed for SAR image segmentation. A Markov random field model on the region adjacency graph was defined in [17] so that the erroneous segmentation caused by speckle noise in SAR imagery can be avoided and the number of configurations for combinatorial optimization can be reduced. A discontinuity-adaptive MRF (DA-MRF) model was developed in [18] to penalize irregularities but accounts for strong discontinuities.

Manuscript received March 1, 2009; revised June 17, 2009 and August 18, 2009. First published January 15, 2010; current version published March 24, 2010.

Y. Li and J. Li are with the Department of Geography and Environmental Management, University of Waterloo, Waterloo, ON N2L 3G1, Canada (e-mail: y62li@uwaterloo.ca; junli@uwaterloo.ca).

M. A. Chapman is with the Department of Civil Engineering, Ryerson University, Toronto, ON M5B 2K3, Canada (e-mail: mchapman@ryerson.ca).

Digital Object Identifier 10.1109/TGRS.2009.2033588

The DA-MRF model integrates the gamma distribution in an objective function for SAR image segmentation. In [19], a simple MRF model with a new implementation scheme was proposed for unsupervised segmentation based on image features. In their new implementation scheme, a function-based weighting parameter between the two components in the traditional two-component MRF model is introduced. In [20], a hidden-class-label MRF model in the wavelet domain was proposed to suppress the effect of speckle noise. They used multiscale segmentation with overlapping window to segment the finest scale of the stationary wavelet transform domain.

We aim to develop a novel region-based approach to SAR image-segmentation-based MRFs. It follows the Bayesian paradigm for image processing [21] and consists of four stages: 1) The construction of prior probability distribution for capturing general and scene-specific knowledge about a given SAR image and is governed by an unknown set of parameters. By Voronoi tessellation, the domain of the given SAR image is partitioned into a set of polygons corresponding to the components of the segmented homogenous regions. Associated with each polygon is a label indicating the homogenous region to which the polygon belongs. The labels for all the polygons form a label field that is modeled by a Markov random field model. 2) The formation of the joint probability density function (pdf) for SAR image representation called the likelihood. The intensities of pixels in each homogenous region are modeled by a strictly stationary random field (RF), in which their intensities are considered to satisfy identical and independent gamma distributions. 3) The combination of prior distribution and the likelihood by Bayes' theorem to form the posterior distribution of labels, partitions, and distribution parameters conditional on the SAR imagery. 4) The creation of an inference about the labels based on the posterior distribution. A reversible jump Markov chain Monte Carlo (RJMCMC) algorithm is employed to simulate the posterior distribution, and the maximum *a posteriori* (MAP) scheme is used to find the optimal segmentation.

The remainder of this paper is organized as follows: Section II details the proposed segmentation algorithm. Section III presents and discusses the experimental results obtained using real and simulated SAR image, respectively. Section IV draws some conclusions and addresses future aspects of this research.

II. Description of Proposed Algorithm

A. Partition Model

The microwave scattered from a spatial domain $D \subset R^2$ can be expressed by a bivariate random function $Z(x,y)$, where $(x,y) \in D$ is a spatial location in the image domain D. Digitization of the function $Z(x,y)$ is a process of discretely sampling all possible locations and gives rise to a set of random variables, which is called a RF, $\boldsymbol{Z} = \{Z_i = Z(x_i,y_i); i = 1,2,\ldots,n\}$, where n is the number of sampling points (pixels), i is the index of sampling points, and (x_i,y_i) are the georeferenced ground points regularly arranged on D. Therefore, a given SAR image can be viewed as a realization of the RF $\boldsymbol{Z}$.

In this paper, a Voronoi tessellation [22] is explored for partitioning D into subregions. Given a set of points, which are called generating points, $\boldsymbol{G} = \{(u_j,v_j) \in D; j = 1,\ldots,m\}$, where m is the number of generating points, the Voronoi tessellation divides D into a set of polygons, which are called Voronoi polygons, $\boldsymbol{P} = \{P_j; j = 1,\ldots,m\}$, in which the jth Voronoi polygon P_j associated with the generating point (u_j,v_j) consists of the points nearest to (u_j,v_j) than to any other generating point in $\boldsymbol{G}$, i.e.,

$$P_j = \Big\{(x,y) \in D; |(x,y)-(u_j,v_j)| < \min_{(u_{j'},v_{j'}) \in G/(u_j,v_j)} |(x,y)-(u_{j'},v_{j'})| \Big\} \quad (1)$$

where P_j is the convex polygon bounded by a set of bisectors for the links of pairs of generating points [22], [23].

B. Image Model

Assume that a SAR image contains a known number of homogeneous regions k and is partitioned into an unknown number of polygons m *a priori* by Voronoi tessellation, where m possesses a prior distribution with pdf $p(m)$. Associated with each polygon, there is a random label variable that indicates the homogenous region to which the polygon belongs, and label variables for all polygons form a label field $\boldsymbol{L} = \{L_j; j = 1,\ldots,m\}$. A realization of $\boldsymbol{L}$, $\boldsymbol{l} = \{l_j \in \{1,\ldots,k\}; j = 1,\ldots,m\}$, corresponds to a segmentation of the image. In a given polygon P_j, the intensity values of pixels $\boldsymbol{Z}_j = \{Z_i; (x_i,y_i) \in P_j\}$ are conditionally characterized by identical and independent gamma distributions on the label $L_j = l_j$ with the pdf as follows:

$$p(\boldsymbol{Z}_j|L_j,\boldsymbol{\theta}_{l_j}) = \prod_{(x_i,y_i)\in P_j} \frac{1}{\Gamma(\alpha_{l_j})} \beta_{l_j}^{-\alpha_{l_j}} Z_i^{\alpha_{l_j}-1} \exp\left(-\frac{Z_i}{\beta_{l_j}}\right) \quad (2)$$

where $\boldsymbol{\theta}_{lj} = (\alpha_{lj},\beta_{lj})$ is the parameter vector, and α_{lj} and β_{lj} are the shape and scale parameters of the gamma distribution, respectively. The joint pdf of $\boldsymbol{Z}$, given m, $\boldsymbol{L}$, $\boldsymbol{G}$, and the parameters of gamma distributions for all homogeneous regions, becomes

$$\begin{aligned} p(\boldsymbol{Z}|m,\boldsymbol{L},\boldsymbol{G},\boldsymbol{\theta}) &= \prod_{j=1}^{m} p(\boldsymbol{Z}_j|L_j,\boldsymbol{\theta}_{l_j}) \\ &= \prod_{l=1}^{k} \prod_{(x_i,y_i)\in\Delta_l} \frac{1}{\Gamma(\alpha_l)} \beta_l^{-\alpha_l} Z_i^{\alpha_l-1} \exp\left(-\frac{Z_i}{\beta_l}\right) \end{aligned} \quad (3)$$

where $\boldsymbol{\theta}$ is the gamma distribution parameter vector, i.e., $\boldsymbol{\theta} = \{\boldsymbol{\theta}_l = (\alpha_l,\beta_l); l = 1,\ldots,k\}$, and Δ_l is the set of polygons with the same label l, i.e., $\Delta_l = \{P_j; l_j = l, j = 1,\ldots,m\}$.

C. Bayesian Model

Using Bayes' rule, the posterior distribution of m, $\boldsymbol{L}$ $\boldsymbol{G}$, and $\boldsymbol{\theta}$ given $\boldsymbol{Z}$ can be written as

$$p(m,\boldsymbol{L},\boldsymbol{G},\boldsymbol{\theta}|\boldsymbol{Z}) \propto p(\boldsymbol{Z}|m,\boldsymbol{L},\boldsymbol{G},\boldsymbol{\theta}) p(\boldsymbol{G}|m) p(\boldsymbol{\theta}) p(\boldsymbol{L}|m) p(m). \quad (4)$$

In (4), assume that $\boldsymbol{\theta}$ is independent of $\boldsymbol{L}$ and m. To model the correlation of labels for neighbor polygons, the stationary second-order Potts model is used [24], [25]. Given a polygon P_j, let $N_j = (j'; P_j \sim P_{j'})$, j, $j' \in \{1, 2, \ldots, m\}$ and $j' \neq j$, be the set of labels for its neighbor polygons, where the operator $\sim$ donates a neighborhood relationship. The polygons P_j and $P_{j'}$ are neighbors $P_j \sim P_{j'}$ if and only if P_j and $P_{j'}$ share a mutual boundary. The conditional distribution of the label variable for the polygon P_j given the labels of its neighbor polygons can be expressed as

$$p(L_j|L_{j'}, j' \in N_j) = \frac{\exp\left(c \sum\limits_{j' \in N_j} t(L_j, L_{j'})\right)}{\sum\limits_{l=1}^{k} \exp\left(c \sum\limits_{j' \in N_j} t(l, L_{j'})\right)} \tag{5}$$

where $c > 0$ is a constant that controls the neighborhood dependences between a pair of neighbor polygons [26], and t is an indicator function, i.e.,

$$t(x, y) = \begin{cases} 1, & \text{if } x = y \\ 0, & \text{otherwise.} \end{cases} \tag{6}$$

The joint pdf of the label field $\boldsymbol{L}$ can be expressed as

$$\begin{aligned} p(\boldsymbol{L}|m) &= \prod_{j=1}^{m} p(L_j|L_{j'}, j' \in N_j) \\ &= \prod_{j=1}^{m} \frac{\exp\left(c \sum\limits_{j' \in N_j} t(L_j, L_{j'})\right)}{\sum\limits_{l=1}^{k} \exp\left(c \sum\limits_{j' \in N_j} t(l, L_{j'})\right)}. \end{aligned} \tag{7}$$

However, if some interaction between generating points is necessary, then the following processes that model the interaction can be considered, such as Gaussian perturbed points [27], the nearest-neighbor Markov process [28], and the Strauss process [29]. The prior distribution for the number of generating points is assumed to satisfy the Poisson distribution with a mean λ. Its pdf can be written as

$$p(m) = \frac{\lambda^m}{m!} \exp(-\lambda). \tag{8}$$

The shape and scale parameters of the gamma distribution are assumed to be identical independent Gaussian distributions, i.e., $\alpha \sim N(\xi, \kappa)$, and truncated $\alpha > 0$, $\beta \sim N(\omega, \gamma)$, where ξ, κ, ω, and γ are constants. The joint pdf's of $\boldsymbol{\alpha} = \{\alpha_l; l = 1, \ldots, k\}$ and $\boldsymbol{\beta} = \{\beta_l; l = 1, \ldots, k\}$ can be written, respectively, as

$$p(\boldsymbol{\alpha}) = \prod_{l=1}^{k} \frac{1}{\sqrt{2\pi}\kappa} \exp\left[-\frac{(\alpha_l - \xi)^2}{2\kappa^2}\right] \tag{9}$$

$$p(\boldsymbol{\beta}) = \prod_{l=1}^{k} \frac{1}{\sqrt{2\pi}\gamma} \exp\left[-\frac{(\beta_l - \omega)^2}{2\gamma^2}\right]. \tag{10}$$

For a generating point (u_j, v_j) uniformly distributed on D, its pdf can be expressed as

$$p(u_j, v_j) = \frac{1}{|D|} \tag{11}$$

where $|D|$ denotes the area of the domain D. Assuming that all the generating points are independently drawn from D, the joint pdf of $\boldsymbol{G}$ is given by

$$p(\boldsymbol{G}|m) = \prod_{j=1}^{m} p(u_j, v_j) = \frac{1}{|D|^m}. \tag{12}$$

The posterior distribution defined in (4) can be rewritten as

$$\begin{aligned} p(m, \boldsymbol{L}, \boldsymbol{G}, \boldsymbol{\theta}|\boldsymbol{Z}) &\propto (\boldsymbol{Z}|m, \boldsymbol{L}, \boldsymbol{G}, \boldsymbol{\theta}) p(\boldsymbol{G}|m) p(\boldsymbol{\theta}) p(\boldsymbol{L}|m) p(m) \\ &= \prod_{l=1}^{k} \prod_{(\boldsymbol{x}_i, y_i) \in \Delta_l} \frac{1}{\Gamma(\alpha_l)} \beta_l^{-\alpha_l} Z_i^{\alpha_l - 1} \exp\left(-\frac{Z_i}{\beta_l}\right) \\ &\quad \times \prod_{j=1}^{m} \frac{\exp\left(c \sum\limits_{j' \in N_j} t(L_j, L_{j'})\right)}{\sum\limits_{l=1}^{k} \exp\left(c \sum\limits_{j' \in N_j} t(l, L_{j'})\right)} \\ &\quad \times \prod_{l=1}^{k} \frac{1}{\sqrt{2\pi}\kappa} \exp\left[-\frac{(\alpha_l - \xi)^2}{2\kappa^2}\right] \\ &\quad \times \prod_{l=1}^{k} \frac{1}{\sqrt{2\pi}\gamma} \exp\left[-\frac{(\beta_l - \omega)^2}{2\gamma^2}\right] \\ &\quad \times \frac{\lambda^m}{m!} \exp(-\lambda) \times \frac{1}{|D|^m}. \end{aligned} \tag{13}$$

D. Simulation

To segment a SAR image, it is necessary to simulate from the posterior distribution defined in (13) and estimate its parameters. Let $\boldsymbol{\Theta} = (m, \boldsymbol{L}, \boldsymbol{G}, \boldsymbol{\theta})$ be the parameter vector of the posterior distribution. It is noteworthy that when m is a variable, the dimension of the parameter vector $\boldsymbol{\Theta}$ varies. In this paper, the RJMCMC algorithm [30] is used to simulate dependent samples from the posterior distribution of $\boldsymbol{\Theta}$, whereas the parameter space is variable during sampling. According to Green [30], a new candidate $\boldsymbol{\Theta}^*$ for $\boldsymbol{\Theta}$ is proposed at each iteration by an invertible deterministic function $\boldsymbol{\Theta}^* = \boldsymbol{\Theta}^*(\boldsymbol{\Theta}, \boldsymbol{s})$ (assume that the dimension of $\boldsymbol{\Theta}^*$ is higher than that of $\boldsymbol{\Theta}$), where $\boldsymbol{s}$ is a random vector defined for accomplishing a transition from $(\boldsymbol{\Theta}, \boldsymbol{s})$ to $\boldsymbol{\Theta}^*$ with the dimension satisfying the dimension matching condition, i.e., $|\boldsymbol{\Theta}| + |\boldsymbol{s}| = |\boldsymbol{\Theta}^*|$ [30]. The appropriate acceptance probability for the proposed transition from $\boldsymbol{\Theta}$ to $\boldsymbol{\Theta}^*$ is given by

$$\alpha(\boldsymbol{\Theta}, \boldsymbol{\Theta}^*) = \min\left\{1, \frac{p(\boldsymbol{\Theta}^*|\boldsymbol{Z}) r(\boldsymbol{\Theta}^*)}{p(\boldsymbol{\Theta}|\boldsymbol{Z}) r(\boldsymbol{\Theta}) q(\boldsymbol{s})} \left|\frac{\partial(\boldsymbol{\Theta}^*)}{\partial(\boldsymbol{\Theta}, \boldsymbol{s})}\right|\right\} \tag{14}$$

where $q(\boldsymbol{s})$ is the pdf of $\boldsymbol{s}$, and $r(\boldsymbol{\Theta}^*)$ and $r(\boldsymbol{\Theta})$ are the probabilities of a given move type in states $\boldsymbol{\Theta}^*$ and $\boldsymbol{\Theta}$, respectively.

The Jacobian $|\partial(\boldsymbol{\Theta}^*)/\partial(\boldsymbol{\Theta}, \boldsymbol{s})|$ is due to the change of variable from $(\boldsymbol{\Theta}, \boldsymbol{s})$ to $\boldsymbol{\Theta}^*$.

The move types designed in this paper include the following:

Move 1: updating gamma distribution parameters. The parameter vector for gamma distributions can be written as $\boldsymbol{\theta} = \{\boldsymbol{\theta}_l; l = 1, \ldots, k\}$, where $\boldsymbol{\theta}_l = (\alpha_l, \beta_l)$. Assume that the probability distributions for the proposals α_l^* and β_l^* are Gaussian distributions with means α_l and β_l and standard differences ε_α and ε_β, respectively, i.e., $\alpha_l^* \sim N(\alpha_l, \varepsilon_\alpha)$ and $\beta_l^* \sim N(\beta_l, \varepsilon_\beta)$. The acceptance probability for the proposals α_l^* and β_l^* can be obtained as

$$a_{\alpha,\beta}\left(\boldsymbol{\theta}_l, \boldsymbol{\theta}_l^*\right) = \min\left\{1, \prod_{j \in J_l} \frac{p\left(\boldsymbol{Z}_j|\boldsymbol{\theta}_l^*\right) \times p\left(\boldsymbol{\theta}_l^*\right)}{p(\boldsymbol{Z}_j|\boldsymbol{\theta}_l) \times p(\boldsymbol{\theta}_l)}\right\} \tag{15}$$

where $J_l = \{j'; l_{j'} = l\}$.

Move 2: updating labels. A polygon P_j with label l_j is randomly drawn. To update its label, a new label l_j^* is then uniformly drawn from $\{1, \ldots, k\}$. The acceptance probability for l_j^* can be written as

$$\alpha_l\left(l_j, l_j^*\right) = \min\left\{1, \frac{\prod_{(\mathbf{x}_i, y_i) \in P_j} \frac{1}{\Gamma\left(\alpha_{l_j^*}\right)} \beta_{l_j^*}^{-\alpha_{l_j^*}} Z_i^{\alpha_{l_j^*}-1} \exp\left(-\frac{Z_i}{\beta_{l_j^*}}\right)}{\prod_{(\mathbf{x}_i, y_i) \in P_j} \frac{1}{\Gamma(\alpha_{l_j})} \beta_{l_j}^{-\alpha_{l_j}} Z_i^{\alpha_{l_j}-1} \exp\left(-\frac{Z_i}{\beta_{l_j}}\right)} \times \frac{\exp\left(c \sum_{j' \in N_j} t(l_j^*, l_{j'})\right)}{\exp\left(c \sum_{j' \in N_j} t(l_j, l_{j'})\right)}\right\}. \tag{16}$$

Move 3: moving position of generating points. One of the generating points in $\boldsymbol{G} = \{(u_j, v_j); j = 1, \ldots, m\}$ is drawn at random, for example, (u_j, v_j). A proposed generating point (u_j^*, v_j^*) is uniformly drawn from its corresponding polygon P_j. The new generating point gives rise to the local changes of P_j and its neighbor polygons $NP_j = \{P_{j'}; j' \in N_j\}$ to P_j^* and $NP_j^* = \{P_{j'}^*, j' \in N_j\}$. The acceptance probability for the move turns out to be

$$\alpha_{gp}\left((u_j, v_j), \left(u_j^*, v_j^*\right)\right) = \min\left\{1, \frac{\prod_{j' \in \{j, N_j^*\}} \prod_{(x_i, y_i) \in P_{j'^*}} \frac{1}{\Gamma(\alpha_{l_j})} \beta_{l_j^*}^{-\alpha_{l_j^*}} Z_i^{\alpha_{l_j^*}-1} \exp\left(-\frac{Z_i}{\beta_{l_j}}\right)}{\prod_{j' \in \{j, N_j\}} \prod_{(x_i, y_i) \in P_{j'}} \frac{1}{\Gamma(\alpha_{l_j})} \beta_{l_j}^{-\alpha_{l_j}} Z_i^{\alpha_{l_j}-1} \exp\left(-\frac{Z_i}{\beta_{l_j}}\right)}\right\}. \tag{17}$$

Move 4: birth or death of generating points. Suppose that the current number of generating points is m, and let the probabilities of proposing a birth or death operation be b_m or d_m, respectively. Consider a birth operation that increases the number of generating points from m to $m+1$, and assume that the new generating point is identified with $m+1$ and its location (u_{m+1}, v_{m+1}) is uniformly drawn from D. Let the polygon induced by (u_{m+1}, v_{m+1}) be P_{m+1} and its label l_{m+1} is uniformly drawn from $\{1, \ldots, k\}$. The set of labels of P_{m+1}'s neighbor polygons is $N_{m+1} = \{j'; P_{j'} \sim P_{m+1}\}$. The Voronoi tessellation is modified by adding the proposed generating point from $\boldsymbol{P} = \{P_1, \ldots, P_{j'}, \ldots, P_m\}$ to $\boldsymbol{P}^* = \{P_1, \ldots, P_{j'}^*, \ldots, P_m, P_{m+1}\}$, where $j' \in N_{m+1}$.

It is evident that the birth or death of a generating point does not affect the gamma distribution parameters in $\boldsymbol{\theta}$. As a result, the parameter vector for the birth operation becomes $\boldsymbol{\Theta}^* = (k, m+1, \boldsymbol{L}^*, \boldsymbol{G}^*, \boldsymbol{\theta})$, where $\boldsymbol{G}^* = ((u_1, v_1), \ldots, (u_m, v_m), (u_{m+1}, v_{m+1}))$, and $\boldsymbol{L}^* = (L_1, \ldots, L_m, L_{m+1})$. The acceptance probability for the birth operation can be written as

$$\alpha_b(\boldsymbol{\Theta}, \boldsymbol{\Theta}^*) = \min\{1, R_b\} \tag{18}$$

where

$$R_b = \frac{p(\boldsymbol{Z}|m+1, \boldsymbol{L}^*, \boldsymbol{G}^*, \boldsymbol{\theta}) p(m+1) p(\boldsymbol{G}^*|m+1)}{p(\boldsymbol{Z}|m, \boldsymbol{L}, \boldsymbol{G}, \boldsymbol{\theta}) p(m) p(\boldsymbol{G}^*|m+1)} \times \frac{p(\boldsymbol{L}^*|m+1) r_{b_m}(\boldsymbol{\Theta}^*)}{p(\boldsymbol{L}|m) r_{d_{m+1}}(\boldsymbol{\Theta}) q(\boldsymbol{s})} \left|\frac{\partial(\boldsymbol{\Theta}^*)}{\partial(\boldsymbol{\Theta}, \boldsymbol{s})}\right| \tag{19}$$

where $r_{bm} = b_m$, $r_{dm+1} = d_{m+1}/(m+1)$, $\boldsymbol{s} = l_{m+1}$, and the other terms in (19) can be expressed as

$$\frac{p(\boldsymbol{Z}|m+1, \boldsymbol{L}^*, \boldsymbol{G}^*, \boldsymbol{\theta})}{p(\boldsymbol{Z}|m, \boldsymbol{L}, \boldsymbol{G}, \boldsymbol{\theta})} = \frac{\prod_{j \in \{m+1, N_{m+1}\}} \prod_{(x_i, y_i) \in P_j} \frac{1}{\Gamma(\alpha_{l_j})} \beta_{l_j^*}^{-\alpha_{l_j^*}} Z_i^{\alpha_{l_j^*}-1} \exp\left(-\frac{Z_i}{\beta_{l_j}}\right)}{\prod_{j \in N_{m+1}} \prod_{(x_i, y_i) \in P_j} \frac{1}{\Gamma(\alpha_{l_j})} \beta_{l_j}^{-\alpha_{l_j}} Z_i^{\alpha_{l_j}-1} \exp\left(-\frac{Z_i}{\beta_{l_j}}\right)} \tag{20}$$

$$\frac{p(\boldsymbol{L}^*|m+1)}{p(\boldsymbol{L}|m)} = \frac{\prod_{j \in \{m+1, N_{m+1}\}} \frac{\exp\left(c \sum_{j' \in N_j^*} t(l_j, l_{j'})\right)}{\sum_{l=1}^{k} \exp\left(c \sum_{j' \in N_j^*} t(l, l_{j'})\right)}}{\prod_{j \in N_{m+1}} \frac{\exp\left(c \sum_{j' \in N_j} t(l_j, l_{j'})\right)}{\sum_{l=1}^{k} \exp\left(c \sum_{j' \in N_j} t(l, l_{j'})\right)}} \tag{21}$$

$$\frac{p(m+1)}{p(m)} = \frac{\lambda}{m+1}; \quad \frac{p(\boldsymbol{G}^*|m+1)}{p(\boldsymbol{G}|m)} = \frac{1}{|D|}; \quad \left|\frac{\partial(\boldsymbol{\Theta}^*)}{\partial(\boldsymbol{\Theta}, \boldsymbol{s})}\right| = 1; \quad q(\boldsymbol{s}) = \frac{1}{k}. \tag{22}$$

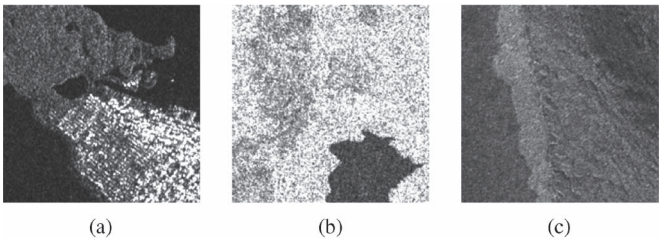

Fig. 1. Satellite SAR images used for testing the proposed algorithm.

The acceptance probability for the death of generating point is given by

$$\alpha_d(\boldsymbol{\Theta}, \boldsymbol{\Theta}^*) = \min\{1, R_d\} \quad \text{and} \quad R_d = R_b^{-1}. \tag{23}$$

For any given proposal with acceptance probability α, it is accepted if and only if $\alpha \geq \eta$, where η is uniformly drawn from [0, 1], i.e., $\eta \sim U(0, 1)$.

E. Optimization for Segmentation

Assume that a set of approximate and dependent samples $\{\boldsymbol{\Theta}^{(t)}, t = 1, \ldots, T_m\}$, where T_m is the number of predefined iterations, is drawn from the joint pdf $p(\boldsymbol{\Theta}|\boldsymbol{Z})$ by the RJMCMC scheme. The MAP estimation [31] is used to obtain optimal parameters defined in the joint pdf. The optimal segmentation represented by the label field $\boldsymbol{L}_{\text{MAP}}$ under the MAP estimate can be written as

$$\boldsymbol{L}_{\text{MAP}} = \arg\max\{p(m, \boldsymbol{L}, \boldsymbol{G}, \boldsymbol{\theta}|\mathbf{z})\}. \tag{24}$$

III. Experimental Results and Discussion

The proposed algorithm is tested with three real Radarsat-1/2 SAR images. In addition, a simulated SAR image is also used to quantitatively evaluate the proposed algorithm.

A. Real SAR Imagery

Fig. 1 shows three real Radarsat-1/2 SAR images with dimensions of 256 × 256 pixels. Among them, part (a) presents a Radarsat-2 standard mode image with HV polarization and spatial resolution of 25 m, which covers part of Stanley Park, Vancouver, British Columbia, Canada, including urban area (white), forest (gray), and waters (black); and part (b) shows a Radarsat-1 image of a coastal scene with VV polarization and spatial resolution of 30 m. Visually, both of them include three homogeneous regions. Part (c) also presents a Radarsat-1 4-look image with VV polarization and spatial resolution of 50 m, which reveals four types of sea ice structures in Ungava Bay, Quebec, Canada. In the remainder of this paper, we use a, b, and c indicate the test images shown in Fig. 1(a)–(c), and 1, 2, 3, and 4 denote the homogenous regions in the decreasing order of their means in each test image.

The constants used for testing the proposed segmentation algorithm are listed in Table I.

The constant c is the coefficient for characterizing the dependence of neighbor polygons in the improved Potts model defined in (5), in which the conditional probability of the label

TABLE I
Constant Used to Test the Proposed Algorithm

Image	c	ξ	κ	ω	γ	λ	ε_α	ε_β	k
a	1	4	0.5	32	4	96	0.5	1	3
b									3
c									4

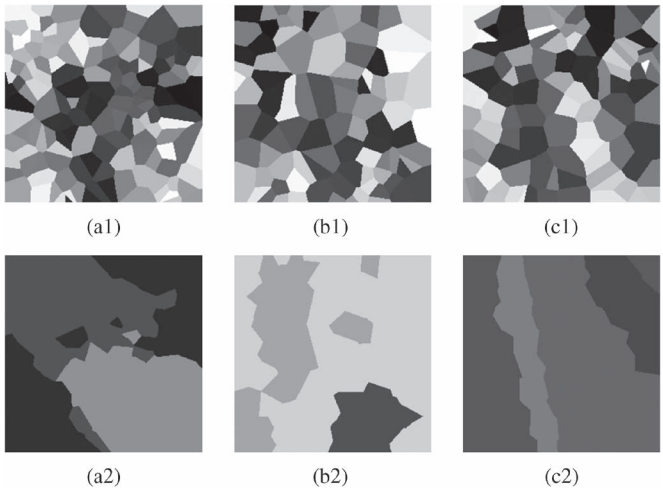

Fig. 2. Results of final partition (a1)–(c1) and optimal segmentation (a2)–(c2).

for a polygon is a monotonic function of c. Depending on the labels for the polygon and its neighbor polygons, the function would be monotone increasing or decreasing with c. From a number of experiments, the interval [0.5, 1.5] for the constant c is recommended. In this experiment, the constant c is set to be 1. The constants ξ and ω are the means of shape parameter α and scale parameter β of the gamma distributions in (2) and (3), respectively, i.e., $\xi = \mathrm{E}(\alpha)$ and $\omega = \mathrm{E}(\beta)$, where $\mathrm{E}(\cdot)$ is the mean operator. Given a multilook SAR image in which the intensities of pixels are characterized by gamma distribution, the shape parameter α is equal to the number of its looks. In this paper, since α is considered as a random variable, the value ξ is set as the number of looks. For a gamma distribution with shape parameter α and scale parameter β, the product of the two parameters $\alpha \cdot \beta$ is equal to its mean. Then, the value $\xi \cdot \omega = \mathrm{E}(\alpha)\mathrm{E}(\beta) = \mathrm{E}(\alpha \cdot \beta)$ (the last equation is true, since α and β are independent) is taken $128 = 256/2$ (i.e., the midpoint of 256 gray levels) since the pixel intensities in a gray-scale image vary in the range of 0 and 255. The constant λ is the mean of a Poisson distribution from which the number of generating point m is drawn. In a certain range, the value of λ does not affect the segmentation results. The constants ε_α and ε_β are the proposal variances for α and β, respectively, which affect the sampling and convergence of the algorithm under the Markov chain Monte Carlo scheme [26]. It was suggested in [32] to choose the proposal variances so that the acceptance probability lies in the interval (0.3–0.7). However, we have found that the proposal variances causing the acceptance probability of around 0.1 still make the algorithm work well. For simplicity, the number of homogeneous regions k for the scene presented in a SAR image is determined by manual inspection *a priori*. In practice, selecting the number is not very reliable as it depends on the experience of human operators and is sometimes impossible since the ground true is always

TABLE II
ESTIMATED PARAMETERS

Image	α_1	α_2	α_3	α_4	β_1	β_2	β_3	β_4
a	3.5	5.7	12.7	-	40.7	11.7	2.0	-
b	10.7	10.2	17.8	-	6.0	16.3	11.9	-
c	4.2	4.5	5.6	6.2	13.9	16.5	16.5	19.1

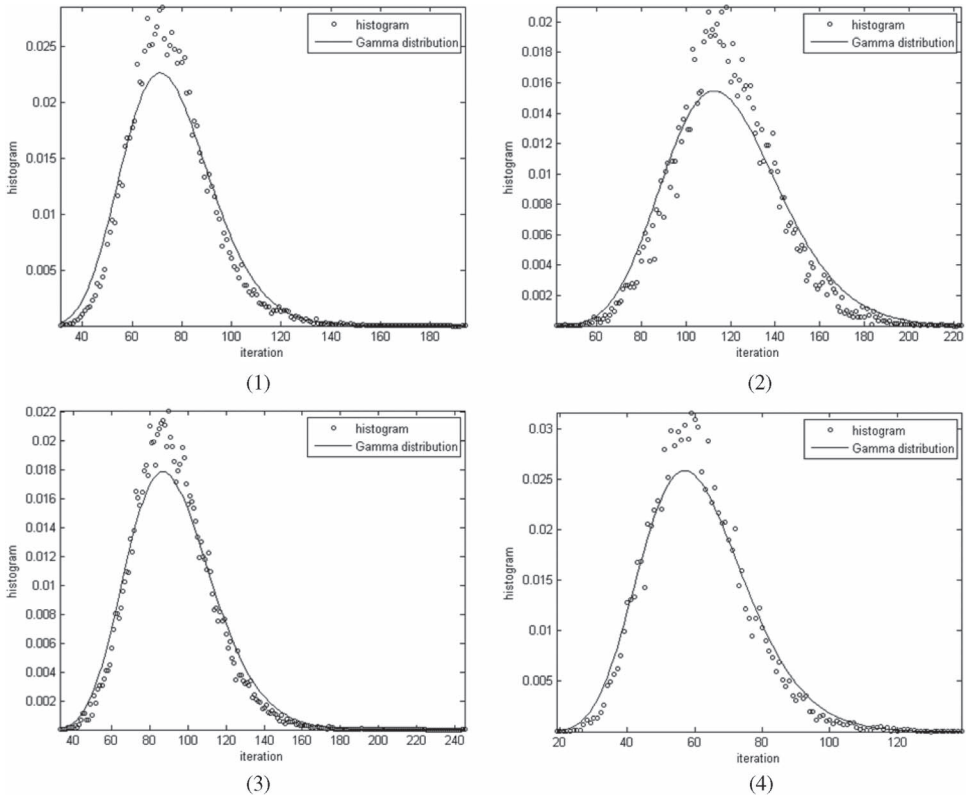

Fig. 3. Histograms and gamma distributions with estimated parameters of segmented regions (1, 2, 3, and 4) in test image Fig. 1(c).

unknown in advance. Therefore, an algorithm for automatically identifying the number of homogenous regions is necessary.

The initial partitions of image domain D are carried out by Voronoi tessellation, in which the number of generating points m_0 is drawn from the Poisson distribution with the mean of 96, and the locations of m_0 generating points are uniformly drawn from D. The initial segmentation is performed by randomly assigning a label to each polygon in the initial partition of D from the Bernoulli distribution with probabilities $p_j = 1/k$, where $j = \{1, \ldots, m\}$, and k is the number of homogeneous regions in each test image. We found that there is no notable impact of the initial segmentation on the final segmentation. Fig. 2(a1), (b1), and (c1) shows the results of the final partitions of D with 146, 140, and 104 polygons, respectively. Fig. 2(a2), (b2), and (c2) shows the results of the optimal segmentation in terms of the MAP estimation after all iterations obtained at the 7997th, 3978th, and 3984th out of a total of 4000 iterations, respectively, where the tone of each region is represented by its estimated mean.

Table II summarizes estimated shape parameters $\alpha_{1,\ldots,k}$ and scale parameters $\beta_{1,\ldots,k}$ for the gamma distributions corresponding to the segmented homogenous regions.

Figs. 3 and 4 shows the histogram of intensities and gamma distributions with the estimated shape and scale parameters of the segmented homogeneous regions for test images (a) and (b) in Fig. 4 and for test image (c) in Fig. 3. As shown in Fig. 4(a1) and (b1), the curves of gamma distributions for regions with maximum estimated means do not fit their histograms well. As shown in Fig. 1(a) and (b), there are many light pixels in these regions, which make the distributions of intensities in the regions out of gamma distributions. Nevertheless, our algorithm still accurately identifies these regions. In other cases, the histograms match the gamma distributions well.

For a visual assessment of whether the result is accurate, the outlines of the segmented homogeneous regions are delineated and then overlaid on the original images. As shown in Fig. 5, the delineated outlines match those of the real homogenous regions quite well.

B. Simulated SAR Imagery

Fig. 6 shows a simulated SAR image, which is generated based on the partition of a domain, as shown in Fig. 6(a). In the simulated image in Fig. 6(b), the intensity values for pixels in each homogeneous region are drawn from gamma distributions with shape parameters equal to 3, 4, and 5, and the scale parameters equal to 24, 32, and 40, respectively.

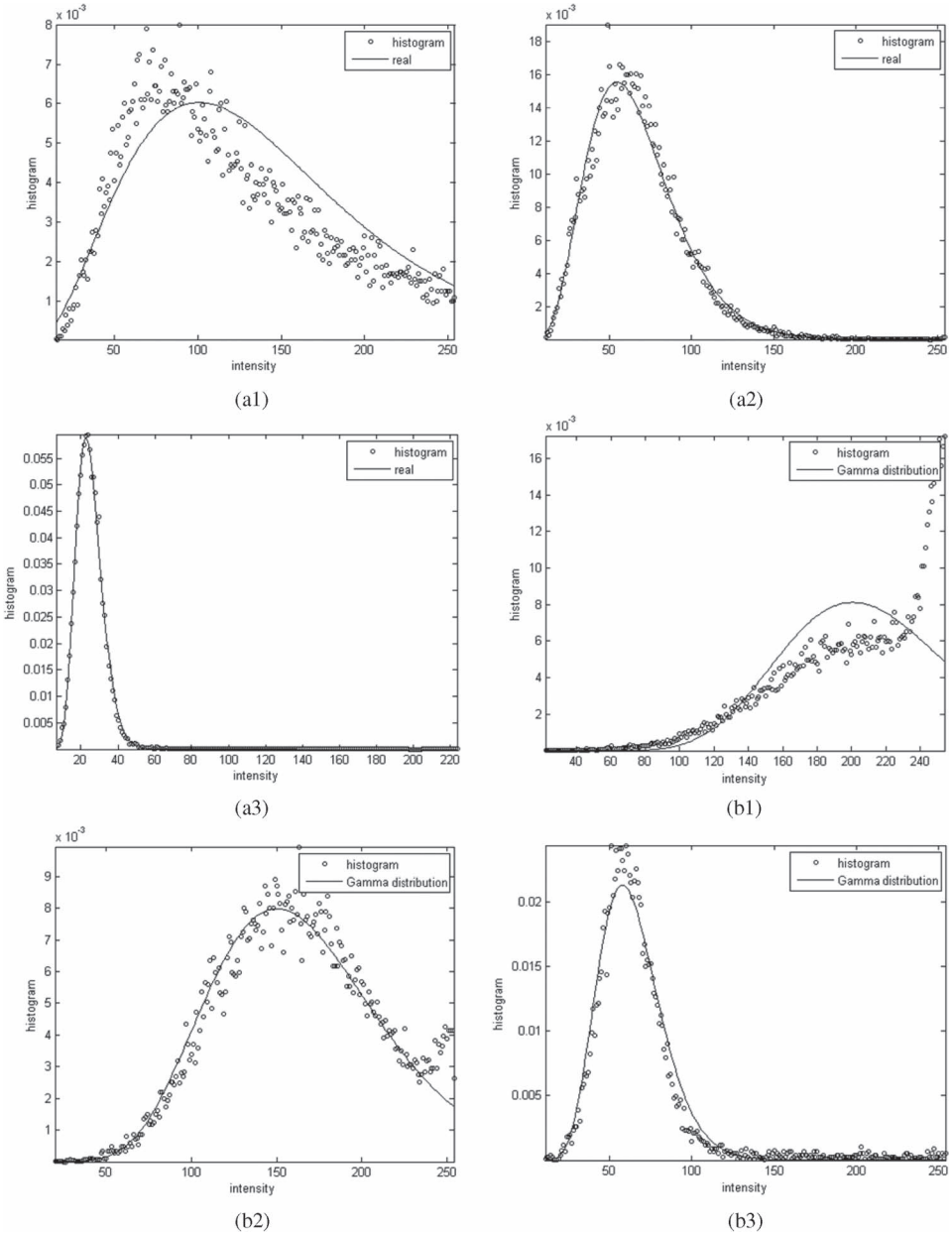

Fig. 4. Histograms and gamma distributions with estimated parameters of segmented regions (1, 2, and 3) in test images in Fig. 1(a) and (b).

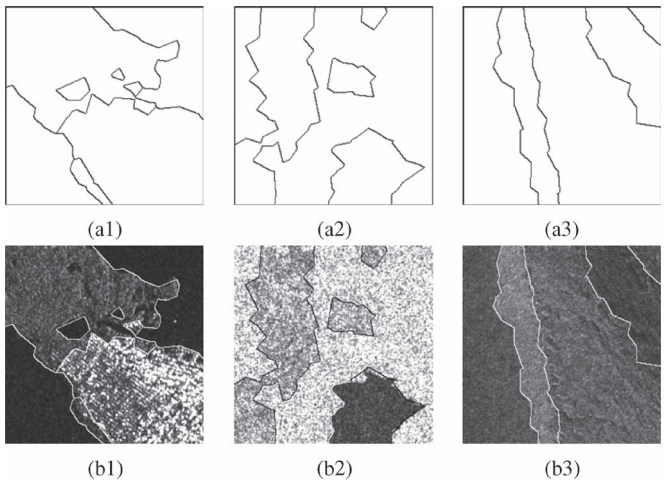

Fig. 5. Delineated outlines (a1)–(c1) and overlaid on test images (a2)–(c2).

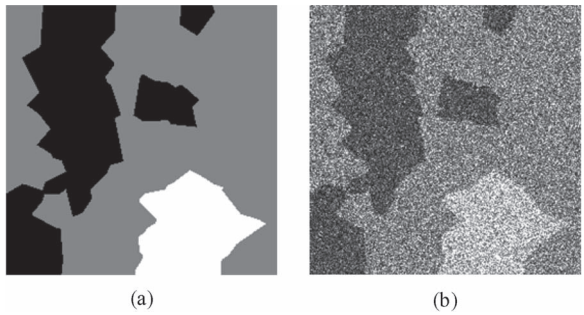

Fig. 6. (a) Partition of domain. (b) Simulated SAR image.

In the experiment using the simulated image, the constants used in our algorithm are the same as those listed in Table I. Fig. 7 shows the changes of the shape and scale parameters during 4000 iterations and reveals that the estimated parameters finally converge their stable values.

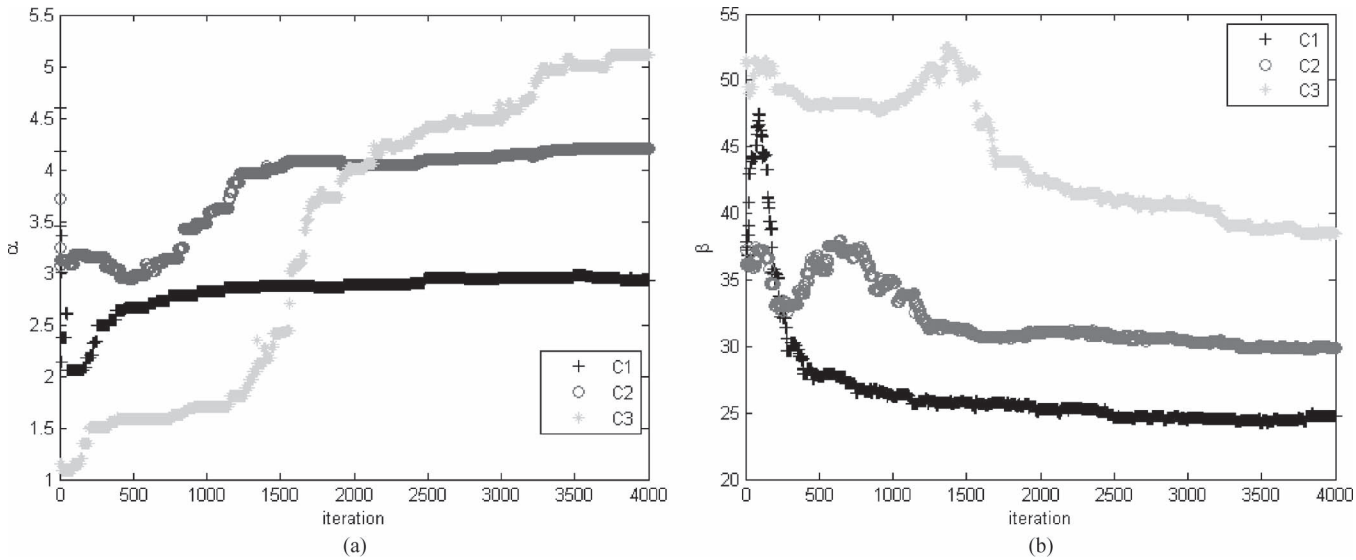

Fig. 7. Changes of estimated (a) shape parameters and (b) scale parameters during 4000 iterations.

TABLE III
ESTIMATED MODEL PARAMETERS AND ERRORS

	C1	C2	C3
α	5.12	4.20	2.93
e_α(%)	2.35	5.00	2.32
β	24.71	29.90	38.53
$e\beta$(%)	3.66	6.55	2.95

Table III gives the estimation values of the shape parameters (α's) and scale parameters (β's) and their percentage error (e_α and e_β), respectively. In Table III, the minimum accuracy of those estimated parameters is larger than 93% ($\approx 100-6.55$). It can be concluded that the estimated values of the shape and scale parameters are close to their real values.

Fig. 8 shows the histograms and gamma distributions with the real and estimated parameters. It can be seen that the histograms and distributions of pixel intensities for each homogeneous region match very well.

Our algorithm was developed using MATLAB running on a DELL Optiple GX 745 computer. The average time spent by one iteration was around 3.6 s, in which all four moves are accepted. As a result, the average computation time for 4000 iterations was about 240 min. The computation burdens for updating the model parameter, updating the label, moving the generating point, and the birth and death of polygon account for 5%, 20%, 35%, and 40%, respectively, since the operations in the experiment for Voronoi tessellation and finding neighbor polygons are time consuming.

In this paper, two assessment schemes are carried out for quantitative evaluation, i.e., the statistical-measure-based scheme [33] and the buffer-zone-based scheme [34]. In the statistical-measure-based scheme, some common measures are used for accuracy assessment, including producer's accuracy, user's accuracy, overall accuracy, and Kappa coefficient [33]. Table IV presents an error matrix, where C1, C2, and C3 indicate the homogenous regions, and ΣCr and ΣCs are the row and column totals. According to this error matrix, the producer's accuracy, the user's accuracy, the overall accuracy, and the Kappa coefficient [33] are calculated. In the worst case, the producer's accuracy of 97.36% of real pixels (7478 out of 7681) in the lightest block on the bottom of the simulated image is correctly segmented. The algorithm incorrectly omitted 2.64% of pixels (203 out of 7681) in the worst case. Correspondingly, the user's accuracy of 97.84% of pixels (7478 out of 7560) segmented in the same region are correctly identified, and only 2.16% of pixels (401 out of 7560) are incorrectly segmented to other homogenous regions. In a similar way, the segmented results for the other homogeneous regions in the simulated image can be evaluated. As a conclusion, the high segmentation accuracy is anticipated when the proposed algorithm is applied. The overall accuracy is 98.28%, and the Kappa coefficient for the segmented result is up to 0.968. According to the general interpretation rules for thematic accuracy assessment, the Kappa coefficients 0.81–1.00 can be interpreted as almost perfect [35].

Another scheme for the accuracy assessment of the proposed algorithm is based on the degree to which the delineated or extracted outlines of the segmented homogeneous regions match their alternatives delineating the real regions, which is measured by the count of pixels of the extracted outlines laying on the buffer zone around the real outlines of the homogenous regions [34]. Fig. 9 shows the extracted outlines (black) of the segmented homogenous regions lying in the buffer zone (gray) with 4-pixel width around the real outlines at each side. It can clearly be seen that almost all of the extracted outlines of the segmented regions lay within the buffer zone.

Table V presents the percentage of extracted outlines on each buffer layer, where B_0 denotes the percentage of extracted outlines of the segmented homogenous region exactly matching the real outlines. The B_i's, where $i = 1, 2, 3, 4$, represent the percentages of extracted outlines of the segmented homogenous regions lying on the ith buffer layer of the real outlines. Table V also shows the accumulated $\Sigma_i = B_0 + B_1 + \cdots + B_i$. Over 80% of the extracted outlines of the segmented homogenous regions are within the buffer zone with one pixel width around the real outlines, and almost all the extracted outlines (around

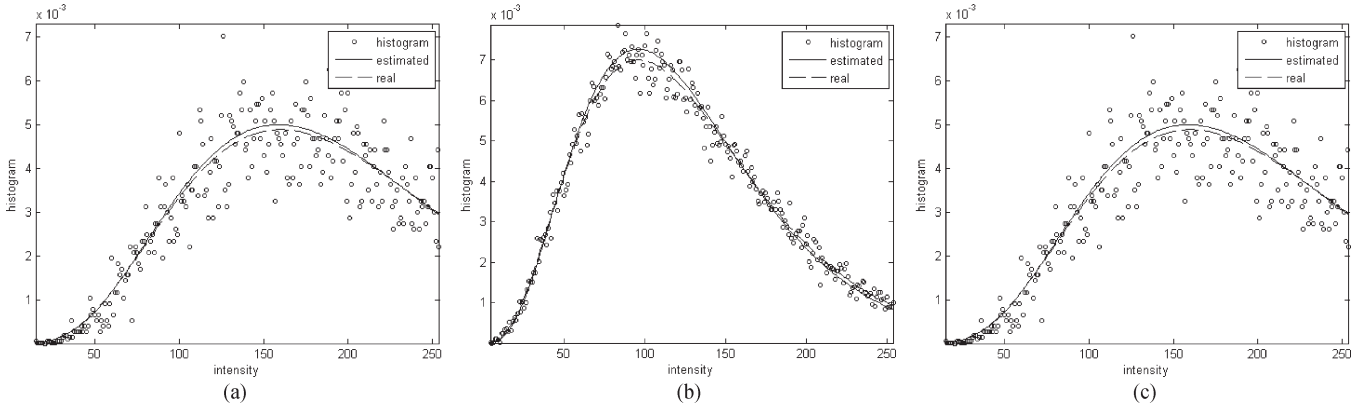

Fig. 8. Histogram and curves of gamma distributions with real and estimated model parameters.

TABLE IV
ERROR MATRIX

	C_1	C_2	C_3	$\sum C_r$
C_1	7478	401	0	7560
C_2	203	38759	477	39439
C_3	0	82	18136	18537
$\sum C_s$	7681	39242	18613	65536

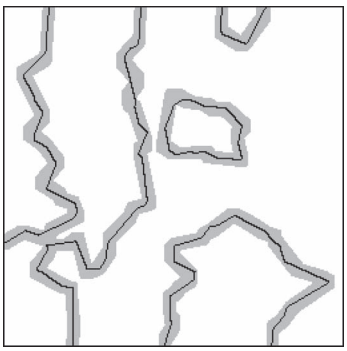

Fig. 9. Extracted outlines overlaid on the buffer zones around the outlines of real regions.

TABLE V
PERCENTS OF THE EXTRACTED OUTLINES ON EACH BUFFER LAYER

B_0 (%)	B_1/Σ_1(%)	B_2/Σ_2(%)	B_3/Σ_3(%)	B_4/Σ_4(%)
43.97	44.08/87.05	9.64/96.68	2.76/99.45	0.55/100.00

99%) are on the buffer zone with 4 pixels in width around the real outlines.

IV. CONCLUSION

The segmentation of satellite SAR intensity imagery is a very challenging task due to the speckle effect. This paper has presented a new segmentation approach based on Voronoi tessellation, the Bayesian inference, and the RJMCMC algorithms. The approach has been evaluated based on extensive experiments using both real Radarsat-1/2 and simulated SAR images. The experimental results show the efficiency of the proposed segmentation approach.

In this paper, the number of homogenous regions existing in SAR imagery is assumed to be known *a priori*. Unfortunately, it is difficult to specify a desired number for homogenous regions *a priori*. In the future work, the number will be considered as a variable. There are two major issues for developing such algorithms: 1) the simulation scheme and 2) label switching. The RJMCMC algorithm [30] is an ideal solution to the simulation scheme because of its ability and flexibility in simultaneously performing model selection and parameter estimation. For the variable number, the numerical labeling of the homogenous regions is arbitrary. For example, the region labeled 1 at a certain point in a time will usually represent a completely different region at a later time. To overcome this problem, some algorithms have been proposed, e.g., ordering the labels in the relative order of the means or variables was considered [36]. A relabeling algorithm using decision theory was proposed [37]. It is also well known that the distribution of homogenous regions in a multilook SAR image can be characterized by gamma, Gaussian, or K distributions. Therefore, it is necessary to investigate SAR image segmentation using those distributions in future work.

ACKNOWLEDGMENT

The authors would like to thank Dr. Z. Ou of the Canadian Ice Service for providing Radarsat-1/2 SAR images and the anonymous reviewers for their valuable comments.

REFERENCES

[1] D. Marr, *Vision: A Computational Investigation into the Human Representation and Processing of Visual Information*. San Francisco, CA: Freeman, 1982.
[2] C. Oliver and S. Quegan, *Understating Synthetic Aperture Radar Images*. Boston, MA: Artech House, 1998.
[3] J. S. Hadamard, *Lectures on the Cauchy's Problem in Linear Partial Differential Equations*. New York: Dover, 1952.
[4] T. Poggio, C. Koch, and V. Torre, "Computational vision and regularization theory," *Nature*, vol. 317, no. 6035, pp. 314–319, Sep. 1985.
[5] J. S. Lee, I. Jurkevich, P. Dewaele, P. Wambacq, and A. Oosterlink, "Speckle filtering of synthetic aperture radar images: A review," *Remote Sens. Rev.*, vol. 8, pp. 313–340, 1994.
[6] L. G. Shapiro and G. C. Stockman, *Computer Vision*. Englewood Cliffs, NJ: Prentice-Hall, 2001.
[7] R. Touzi, A. Lopes, and P. Bousquet, "A statistical and geometrical edge detector for SAR images," *IEEE Trans. Geosci. Remote Sens.*, vol. 26, no. 6, pp. 764–773, Nov. 1988.
[8] D. M. Smith, "Speckle reduction and segmentation of synthetic aperture radar images," *Int. J. Remote Sens.*, vol. 17, no. 11, pp. 2043–2057, Jul. 1996.

[9] J. J. Quan, X. B. Wen, and X. Q. Xu, "Multiscale probabilistic neural network method for SAR image segmentation," *Appl. Math. Comput.*, vol. 205, no. 2, pp. 578–583, Nov. 2008.
[10] R. Fjørtoft, A. Lopes, P. Marthon, and E. Cubero-Castan, "An optimum multiedge detector for SAR image segmentation," *IEEE Trans. Geosci. Remote Sens.*, vol. 36, no. 3, pp. 793–802, May 1998.
[11] O. Germain and P. Refregier, "Edge location in SAR images: Performance of the likelihood ratio filter and accuracy improvement with an active contour approach," *IEEE Trans. Image Process.*, vol. 10, no. 1, pp. 72–78, Jan. 2001.
[12] W. Li, G. B. Benie, D. C. He, S. Wang, D. Ziou, Q. Hugh, and J. Gwyn, "Watershed-based hierarchical SAR image segmentation," *Int. J. Remote Sens.*, vol. 20, no. 17, pp. 3377–3390, Nov. 1999.
[13] F. Galland, N. Bertaux, and P. Refregier, "Minimum description length synthetic aperture radar image segmentation," *IEEE Trans. Image Process.*, vol. 12, no. 9, pp. 995–1006, Sep. 2003.
[14] D. Cremers, M. Rousson, and R. Deriche, "A review of statistical approaches to level set segmentation: Integrating color, texture, motion and shape," *Int. J. Comput. Vis.*, vol. 72, no. 2, pp. 195–215, Apr. 2007.
[15] I. B. Ayed, A. Mitiche, and Z. Belhadj, "Multiregion level-set partition of synthetic aperture radar images," *IEEE Trans. Pattern Anal. Mach. Intell.*, vol. 27, no. 5, pp. 793–800, May 2005.
[16] S. Geman and D. Geman, "Stochastic relaxation, Gibbs distributions, and the Bayesian restoration of images," *IEEE Trans. Pattern Anal. Mach. Intell.*, vol. PAMI-6, no. 6, pp. 721–741, Nov. 1984.
[17] G. S. Xia, C. He, and H. Sun, "Integration of synthetic aperture radar image segmentation method using Markov random field on region adjacency graph," *IET Radar Sonar Navig.*, vol. 1, no. 5, pp. 348–353, Oct. 2007.
[18] P. C. Smits and S. G. Dellepiane, "Synthetic aperture radar image segmentation by a detail preserving Markov random field approach," *IEEE Trans. Geosci. Remote Sens.*, vol. 35, no. 4, pp. 844–857, Jul. 1997.
[19] H. Deng and D. A. Clausi, "Unsupervised image segmentation using a simple MRF model with a new implementation scheme," *Pattern Recognit.*, vol. 37, no. 12, pp. 2323–2335, Dec. 2004.
[20] M. Li, Y. Wu, and Q. Zhang, "SAR image segmentation based on mixture context and wavelet hidden-class-label Markov random field," *Comput. Math. Appl.*, vol. 57, no. 6, pp. 961–969, Mar. 2009.
[21] J. Besag, "Towards Bayesian image analysis," *J. Appl. Stat.*, vol. 16, no. 3, pp. 395–406, 1989.
[22] A. Okabe, B. Boots, and K. Sugihara, *Spatial Tessellations: Concepts and Applications of Voronoi Diagrams*. Chichester, U.K.: Wiley, 1992.
[23] P. J. Green and R. Sibson, "Computing Dirichlet tessellation in the plane," *Comput. J.*, vol. 21, no. 2, pp. 168–173, 1978.
[24] J. Besag, "On the statistical analysis of dirty picture (with discussion)," *J. R. Stat. Soc., B*, vol. 48, no. 3, pp. 259–302, 1986.
[25] D. J. Strauss, "Clustering on coloured lattices," *J. Appl. Prob.*, vol. 14, no. 1, pp. 135–143, Mar. 1977.
[26] I. Dryden, M. R. Scarr, and C. C. Taylor, "Bayesian texture segmentation of weed and crop image using reversible jump Markov chain Monte Carlo methods," *J. R. Stat. Soc., Ser. C, Appl. Stat.*, vol. 52, no. 1, pp. 31–50, Jan. 2003.
[27] I. L. Dryden, M. R. Faghihi, and C. C. Taylor, "Procrustes shape analysis of spatial point pattern," *J. R. Stat. Soc., B*, vol. 59, no. 2, pp. 353–374, 1997.
[28] A. Baddeley and J. Møller, "Nearest neighbour Markov point processes and random sets," *Int. Stat. Rev.*, vol. 57, pp. 89–121, 1989.
[29] B. D. Ripley, *Spatial Statistics*. New York: Wiley, 1981.
[30] J. Green, "Reversible jump Markov chain Monte Carlo computation and Bayesian model determination," *Biometrika*, vol. 82, no. 4, pp. 711–732, 1995.
[31] J. M. Bernardo and A. F. M. Smith, *Bayesian Theory*. New York: Wiley, 1994.
[32] J. Besag, P. Green, D. Higdon, and K. Mengersen, "Bayesian computation and stochastic systems (with discussion)," *Stat. Sci.*, vol. 10, pp. 3–66, 1995.
[33] R. G. Congalton and K. Green, *Assessing the Accuracy of Remotely Sensed Data: Principles and Practices*. Boca Raton, FL: CRC Press, 2008.
[34] Y. Li, J. Li, and Y. Lu, "A fuzzy segmentation based approach to extraction of coastlines from IKNOS imagery," *Geomatica*, vol. 62, no. 4, pp. 396–408, 2008.
[35] J. L. Fleiss, "Measuring agreement between two judges on present or absent of a trait," *Biometrics*, vol. 31, pp. 651–659, 1975.
[36] S. Richardson and P. J. Green, "On Bayesian analysis of mixtures with an unknown number of components (with discussion)," *J. R. Stat. Soc., B*, vol. 59, no. 4, pp. 731–792, 1997.
[37] M. Stephens, "Dealing with label switch in mixture models," *J. R. Stat. Soc., B*, vol. 62, no. 4, pp. 795–809, 2000.

Yu Li received the B.Eng. degree in electronic engineering from Xidian University, Xi'an, China, in 1984 and the M.A.Sc. degree in geomatics engineering from Ryerson University, Toronto, ON, Canada, in 2004. He is currently working toward the Ph.D. degree in geomatics with the University of Waterloo, Waterloo, ON, Canada.

He has published more than 30 papers in refereed journals, books, and proceedings. His research interests are remotely sensed data segmentation and classification, spatial statistics, and its application to image analysis.

Jonathan Li (M'00) received the Ph.D. degree in geomatics engineering from the University of Cape Town, Cape Town, South Africa, in 2000.

He is currently an Associate Professor with the Department of Geography and Environmental Management, University of Waterloo, Waterloo, ON, Canada. He has published more than 150 papers in refereed journals, books, and proceedings, and coedited six books. His current research interests are in the areas of information extraction and cartographic mapping from very high resolution satellite multispectral and SAR imagery as well as LiDAR point clouds.

Michael A. Chapman received the Ph.D. degree in photogrammetry from Laval University, Quebec City, QC, Canada, in 1989.

He is currently a Professor with the Department of Civil Engineering, Ryerson University, Toronto, ON, Canada. He has published more than 100 papers in refereed journals, books, and proceedings. His current research interests include algorithms and processing methodologies for airborne sensors using GPS/INS, geometric processing of digital imagery in industrial environments, terrestrial imaging systems for transportation infrastructure mapping, and algorithms and processing strategies for biometrology applications.